



# Imaging Mueller matrix ellipsometry with sub-micron resolution based on back focal plane scanning

CHAO CHEN,<sup>1</sup> XIUGUO CHEN,<sup>1,2</sup> CAI WANG,<sup>1</sup> SHENG SHENG,<sup>1</sup> LIXUAN SONG,<sup>1</sup> HONGGANG GU,<sup>1,3</sup> AND SHIYUAN LIU<sup>1</sup>

<sup>1</sup>State Key Laboratory of Digital Manufacturing Equipment and Technology, Huazhong University of Science and Technology, Wuhan, Hubei 430074, China

<sup>2</sup>[xiuguo@hust.edu.cn](mailto:xiuguo@hust.edu.cn)

<sup>3</sup>[hongganggu@hust.edu.cn](mailto:hongganggu@hust.edu.cn)

**Abstract:** The development of nanotechnology and nanomaterials has put forward higher requirements and challenges for precision measurement or nanometer measurement technology. In order to cope with this situation, a new type of imaging Mueller matrix ellipsometer (IMME) has been developed. A back focal plane scanning method is designed to make the IMME have the ability to measure multiple incident angles. A two-step calibration method is proposed to ensure the measurement accuracy of IMME. After calibration, the IMME can achieve measurement with wavelengths from 410 nm to 700 nm and incident angles from 0° to 65°. The lateral resolution of the IMME is demonstrated to be 0.8 μm over the entire measurement wavelength range. In addition, a Hadamard imaging mode is proposed to significantly improve the imaging contrast compared with the Mueller matrix imaging mode. Subsequently, the IMME is applied for the measurement of isotropic and anisotropic samples. Experimental results have demonstrated that the proposed IMME has the ability to characterize materials with complex features of lateral micron-distribution, vertical nano-thickness, optical anisotropy, etc., by virtue of its advantages of high lateral resolution and high precision ellipsometric measurement.

© 2021 Optical Society of America under the terms of the [OSA Open Access Publishing Agreement](#)

## 1. Introduction

In recent years, with the development of modern science and technology, the application range of optoelectronics is rapidly extending. Following this, higher requirements are put forward for the performance of optoelectronic devices that are basically made of micro- or nano-scale thin films or structures [1]. In order to deal with the ensuing challenges, optoelectronic devices are gradually developing in the direction of miniaturization, complexity, and efficiency. However, without matching metrology, it is difficult to ensure that these devices can be manufactured in accordance with the design standards. Therefore, developing precise measurement technology is of broad prospects and important significance.

According to practical needs, measurement techniques for micro- or nano-scale thin films and structures can be mainly divided into two categories. One is for geometric shapes and sizes of the thin films and structures, such as atomic force microscopy (AFM) and scanning electron microscopy [2], and the other is for optical properties, such as Raman spectroscopy and X-ray scattering techniques [3,4]. All the means are either destructive or slow in measurement, which makes them cannot meet measurement requirements. Different from the above conventional measurement methods, the ellipsometry has obvious advantages in non-destructive, fast measurement, and simultaneous characterization of the morphology and optical properties simultaneously [5–7]. However, since the ellipsometry detects information of the sample covered by the spot, the measurement results are the average results within the spot when the lateral distribution of the sample is smaller than the detection spot size.

To solve the limitation in lateral resolution in traditional ellipsometry, the imaging ellipsometry (IE) comes into being. The IE combines the ellipsometry with imaging optics, whose detector is changed from a spectrometer to a camera. Each pixel on the camera can be employed as an independent detector for detection and analysis of different areas of the sample. Traditional IE applies oblique mode [8,9], referring from the optical path configuration of the traditional ellipsometer, and inserts the required imaging elements at the incident end and the detection end. The incident end and the detection end do not share the optical path and always have an inclined angle with the sample stage. Recently, there are many researches on IE in oblique mode. K. Joo et al. [10] developed a spectroscopic IE for large area measurements. They used a low numerical aperture objective lens to achieve detection of a large field of view, but at the expense of lateral resolution. A. Komiya et al. [11] developed a three-step phase-shifting IE to measure nanofilm thickness profiles. The achievable spatial resolutions are 1.58  $\mu\text{m}$  and 4.62  $\mu\text{m}$  in the horizontal and vertical directions, respectively. In general, limited by the mechanical interference and the working distance of the objective lens, the lateral resolution of this kind of IE is difficult to exceed 1  $\mu\text{m}$ .

Another form of IE is based on the vertical mode [12,13], referring from the optical path configuration of the optical microscope, and inserts the required polarization elements at the incident end and the detection end. The incident end and the detection end partly or completely share the optical path, and the part of the common optical path is kept perpendicular to the sample stage. By maximizing the use of the numerical aperture of the objective lens, the achievable lateral resolution can be close to the Abbe diffraction limit. Thus, the IE in vertical mode is more capable of measuring samples below the micron level. There are some researches on IE in vertical mode recently. K. Fukuzawa et al. developed a vertical-objective-type ellipsometric microscopy (VEM) [14,15]. The VEM measures the ellipsometric angles with configuration of polarizer-compensator-sample-analyzer. The illumination light is focused and fixed onto an off-axis point on the back focal plane (BFP) of the objective lens before measurement in order to provide a sufficient sensitive ellipsometric signal. O. Arteaga et al. developed a BFP Mueller matrix microscopy [16]. This observation mode provides a flat projection of all light rays passing through the specimen in a three-dimensional space. C. Hu et al. developed an azimuth-dependent reflectance difference microscopy [17]. Due to the appearance of the isotropic layer, the azimuth-dependent reflectance difference microscopy can be used to observe the distribution of small anisotropic patches in the visualized optical image without any interference. S. Y. Lee et al. developed a coaxial spectroscopic snapshot ellipsometry and a coaxial spectroscopic IE [18–20]. They adopted convergent light illumination and parallel light illumination to measure optical properties of isotropic samples.

Each of the above work has its own advantages. However, they cannot fully meet the existing measurement needs. For the measurement of micro-area samples, the system is required to have sufficient lateral resolution and magnification. For ellipsometric measurement, the system is required to be operated at different incident angles, since different samples have different polarization sensitivity angles (namely Brewster angles). For the measurement of samples with anisotropic or depolarization characteristics, the system is required to have the ability to measure the complete Mueller matrix. In order to characterize the sample more comprehensively and accurately, we developed an imaging Mueller matrix ellipsometer (IMME) with sub-micro resolution based on BFP scanning. This paper proceeds with the following content. In Section 2, the hardware configuration and principle of the IMME are explained. In Section 3, the detailed calibration method is described. The verification results of the proposed IMME are presented in Section 4, and several applications of the IMME are given in Section 5. The paper is concluded in Section 6.

## 2. Operation principle

Figure 1 presents the schematic of the proposed IMME. A beam of broad-spectrum light emitted from a supercontinuum laser source (WhiteLase SC-400, NKT Photonics, Inc., Denmark) passes through the monochromator (LLTF, NKT Photonics, Inc., Denmark) and is collected by the collimating lens. This collimated light passes successively through the anti-speckle module, mirror, polarization state generator (PSG), beam splitter, imaging lens, and objective lens (OL, EC Epiplan - Apochromat 50  $\times$  0.95 HD DIC, Zeiss, Inc., Germany). Then, the light is reflected by the sample, and enters the objective lens, imaging lens, beam splitter, polarization state analyzer (PSA), relay lens pair, and the detector (Andor Zyla 5.5, Oxford Instruments, Inc., UK) in turn. To be clear, both PSG and PSA are composed of a polarizer (called analyzer in PSA) and a self-designed superachromatic composite waveplate (used as the rotating compensator) [21]. The incidence plane is a plane jointly determined by the PSG and the PSA, which is perpendicular to the rotation axis of the mirror M. The anti-speckle module is composed of rotating ground glass and vibrating optical fiber, and the corresponding rotation speed and vibration speed are optimized for the best anti-speckle effect.

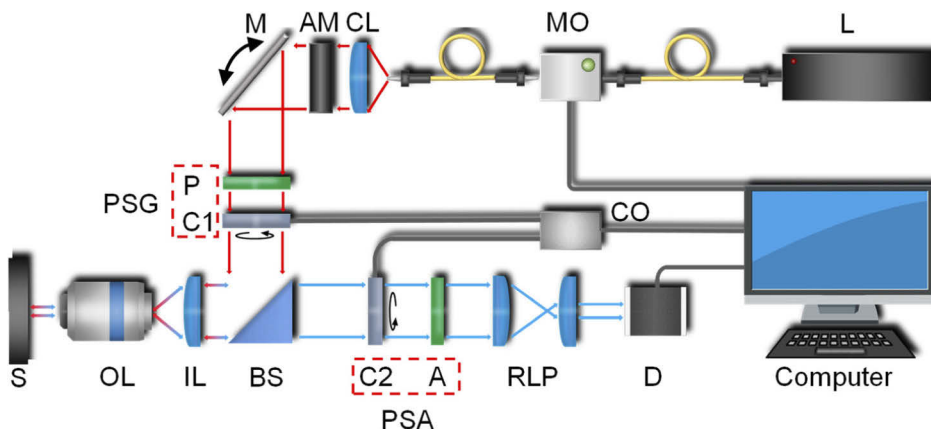


**Fig. 1.** Schematic of the proposed imaging Mueller matrix ellipsometer. L: light source, MO: monochromator, CL: collimating lens, AM: anti-speckle module, M: mirror, P: polarizer, C1: the 1st compensator, BS: beam splitter, IL: imaging lens, OL: objective lens, S: sample stage, C2: the 2nd compensator, A: analyzer, RLP: relay lens pair, D: detector, CO: controller, PSG: polarization state generator, PSA: polarization state analyzer.

The IMME can be divided into three fundamental building blocks: illumination elements, polarization elements and imaging elements. Illumination elements provide homogeneous monochromatic light for sample lighting and detecting. Polarization elements are responsible for modulating and demodulating the polarization state of the beam in the system to achieve ellipsometric measurement. The imaging elements adopt appropriate imaging resolution and magnification, so that each pixel of the detector can independently measure different areas of the sample.

The available spectrum of the IMME covers from 410 nm to 700 nm depending on elements efficiency (such as lenses, beam splitter, detector). The measurement wavelength range of IMME can cover a wider band, when the appropriate elements are selected. A high numerical aperture objective lens is selected to acquire a large range of incident angles and high spatial resolution. The apochromatic relay lens pair is used to ensure that the imaging position will not change due to chromatic aberration issues, and the objective lens is used to set the focus of a ray on the sample surface. The detector is a sCMOS camera with 2560  $\times$  2160 pixels and 6.5  $\mu\text{m} \times$  6.5  $\mu\text{m}$  pixel size.

The ellipsometric measurement is based upon the modulation of the polarization state for both in coming and out coming light beams. The modulated signal is collected in the form of light intensity changed over time  $t$  by the detector, which can be written as [22,23]:

$$I_{\text{out}}(t) = [1 \ 0 \ 0 \ 0] \cdot \mathbf{M}_{\text{PSA}}[A_p, C_2(t), \delta_2] \cdot \mathbf{M}_s \cdot \mathbf{M}_{\text{PSG}}[P_p, C_1(t), \delta_1] \cdot \mathbf{S}_{\text{in}}, \quad (1)$$

where  $\mathbf{M}_{\text{PSA}}$  and  $\mathbf{M}_{\text{PSG}}$  represent the Mueller matrices of PSA and PSG respectively,  $\mathbf{M}_s$  represents the Mueller matrix of the sample, and  $P_p$  and  $A_p$  are the azimuth angles of the polarizer and the analyzer, respectively. We set the two compensators in PSG and PSA synchronously rotating with the speed ratio 5:3 to generate a periodic signal. Thus, real-time azimuth angle of the first and second compensators are  $C_1(t) = 5\omega t - C_1^0$  and  $C_2(t) = 3\omega t - C_2^0$  respectively, where  $\omega$  is fundamental frequency of the rotating compensators and  $C_1^0$  and  $C_2^0$  are initial azimuth angles of the two compensators, respectively.  $\delta_1$  and  $\delta_2$  are the retardance of the first and second compensators, respectively.  $\mathbf{S}_{\text{in}}$ , which is proportional to  $[1 \ 0 \ 0 \ 0]^T$ , represents the Stokes vector of incident light. Then, Fourier analysis is adopted to calculate the Fourier coefficients of the signal, and  $I_{\text{out}}$  is organized into the following form:

$$I_{\text{out}}(t) = I_0 \left[ 1 + \sum_{n=1}^{16} (\alpha_{2n} \cos 2n\omega t + \beta_{2n} \sin 2n\omega t) \right], \quad (2)$$

where  $I_0$ ,  $(\alpha_{2n}, \beta_{2n})$ ,  $n=1, 2, \dots, 16$  are the dc and ac Fourier coefficients. It is noted that since the detector has a certain integration time when collecting the light, the signal actually obtained in the system is an integral of all the light intensity entering the detector within a certain period of time, written as:

$$H_j = \int_{(j-1)\pi/N\omega}^{j\pi/N\omega} I_{\text{out}}(t) dt \quad (j = 1, 2, \dots, N), \quad (3)$$

where  $\pi/\omega$  is the basic optical period of the system, which is evenly divided into  $N$  parts, and here  $H_j$  is called the  $j$ -th *Hadamard component*. In IMME, the integration time of per Hadamard component is set to be  $\sim 20$  ms, and 50 times integrals are performed per optical period. Thus, the imaging Mueller matrix measurement at a single wavelength will take  $\sim 1$  s. Through Fourier analysis of the Hadamard components, the measured Fourier coefficients can be obtained. By matching the measured and theoretical Fourier coefficients pixel by pixel, a set of theoretical Fourier coefficients that are most consistent with the measured Fourier coefficients can be obtained. Then by solving linear functions of these theoretical Fourier coefficients, the Mueller matrix of the sample can be calculated.

We here propose a BFP scanning method to realize different incident angles in the system. As seen in Fig. 2, different points on the BFP correspond to different incident angles. Thus, we change angle of the mirror in Fig. 1 to transform the angle of parallel light entering the imaging lens. Afterwards, the imaging lens would be a relay station to focus the parallel light into different points on the BFP to achieve different incident angles. Theoretically, when the spherical aberration and coma of the imaging lens and objective lens are well corrected, the incident angle  $\theta$  can be expressed by the following formula:

$$\theta = \sin^{-1} \left( \frac{f_{IL}}{f_{OL}} \sin(2\eta) \right). \quad (4)$$

Among them,  $f_{IL}$  and  $f_{OL}$  represent the focal length of the imaging lens and objective lens,  $\eta$  represents the rotation angle of the mirror relative to the initial position (set the position that makes the light propagate along the optical axis as the initial position). The maximum incident angle that can be realized ideally is  $\sin^{-1}(\text{NA})$ , where NA stands for the numerical aperture of the objective lens. It should be pointed out that the incident angle calculated according to Eq. (4) may deviate from the actual, due to factors such as the clearance of the mirror rotatable stage gear.

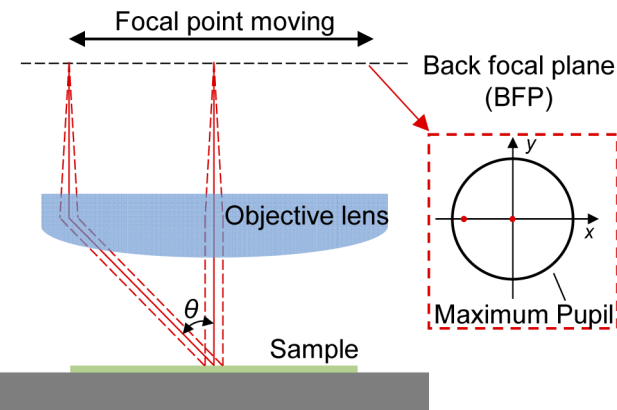


**Fig. 2.** Schematic diagram of back focal plane scanning

### 3. System calibration

#### 3.1. First step calibration

The first step calibration aims at calibrating the polarization elements and beam splitter in the IMME. Although the non-polarized beam splitter is designed with the polarization amplitude taken into consideration, there will still be some linear delay and attenuation remaining. The parameters considered in this step of calibration are the initial azimuth angles of the transmission axes of the polarizer and analyzer, the initial azimuth angles of the fast axes and the wavelength-dependent phase retardance of the first and second compensators, and the wavelength-dependent reflection and transmission polarization effects of the beam splitter.

The specific calibration procedures are as follows. Remove the imaging part in the system. Assemble a 1/4 standard waveplate and a flat mirror as the calibration sample, making optical axes of the 1/4 standard waveplate and the flat mirror coincide, and place the calibration sample in the optical path perpendicular to the incident light, as shown in Fig. 3. As in previous study, the beam splitter shows isotropic properties, and can be described with amplitude ratio and phase difference ( $\Psi_{bt}$ ,  $\Delta_{bt}$ ) in transmission light path and ( $\Psi_{br}$ ,  $\Delta_{br}$ ) in reflection light path, respectively. Another thing to be noted is that under the condition of normal incidence, Mueller matrix of the flat mirror is always a diagonal matrix, namely diag (1, 1, -1, -1) [6], thus the Mueller matrix of the calibration sample is only related to the azimuth angle  $C_{cs}$  and the retardance  $\delta_{cs}$  of the 1/4 waveplate. Then, the Mueller matrix  $\mathbf{M}_s$  in Eq. (1) can be rewritten here as:

$$\mathbf{M}_s = \mathbf{M}_{bt}(\Psi_{bt}, \Delta_{bt})\mathbf{M}_{cs}(C_{cs}, \delta_{cs})\mathbf{M}_{br}(\Psi_{br}, \Delta_{br}), \quad (5)$$

where  $\mathbf{M}_{bt}$  and  $\mathbf{M}_{br}$  represent the Mueller matrices of reflection and transmission polarization effects of the beam splitter, respectively, and  $\mathbf{M}_{cs}$  represents the Mueller matrix of the calibration sample.

After obtaining the light intensity at the initial angle of the calibration sample, change the azimuth angle of the calibration sample at equal intervals by the electric rotating table, and measurement data of multiple periods are continued to be collected to obtain several groups of light intensity information under the azimuth angle of the calibration sample. The number of calibration groups should be more than two. As the number of measurement groups increases, the final fitting result tends to stabilize.

The Fourier analysis can be adopted to calculate the Fourier coefficients of the signal. Then a model with the parameters to be calibrated as the input variables  $\Omega_1 = [A_p, P_p, C_1^0, C_2^0, C_{cs}, \delta_1, \delta_2, \delta_{cs}, \Psi_{bt}, \Delta_{bt}, \Psi_{br}, \Delta_{br}]^T$  and the Fourier coefficients of the signal as the output parameters is

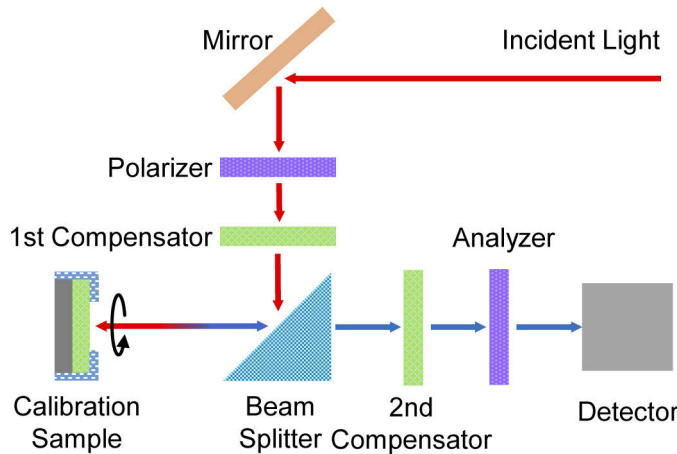


**Fig. 3.** Setup of the first step calibration

established. The model contains 12 unknowns, and 24 non-zero harmonic Fourier coefficients. By solving the following nonlinear least squares optimization problem, the parameter values to be calibrated can be obtained, and the solution process can be optimized by the nonlinear fitting algorithm:

$$\arg \min_{\Omega_1} \sum_{i=1}^{J_1} \|\mathbf{Fc}_i(\Omega_1) - \mathbf{MFc}_i\|_2. \quad (6)$$

Among them,  $J_1$  is the number of rotations of the calibration sample, which needs to satisfy  $J_1 \geq 2$ .  $\mathbf{Fc}$  and  $\mathbf{MFc}$  are  $J_1 \times 24$ -dimensional vectors, and represent the Fourier coefficient obtained by the fitting model and measurement, respectively.  $\|\cdot\|_2$  represents the two-norm of the matrix. Detailed calibration results are given in Appendix A.

### 3.2. Second step calibration

The second step calibration aims at calibrating the polarization effect of the high NA objective lens and determining the relationship between the incident angle and the rotation angle of the mirror (M). Since the numerical aperture of other lenses in the system is too low, it will not affect the polarization state of the light in the system basically, so it is not considered. In this work, to achieve a high lateral resolution and a large range of incident angle, we adopt an objective lens, whose NA = 0.95. Thus, the polarization effect of the objective lens must be considered. Though the objective lens could be characterized offline, an online calibration method would be more accurate since the offline calibration cannot compensate the installation error which will be magnified several times by a high NA objective lens.

For an objective lens, its optical pupil is a rotational symmetric cycle. Each element of Mueller matrix of the objective lens is a cycle similar to the optical pupil. Through simulation, it is found that the polarization effect of the objective lens has a distribution similar to that of certain items of Zernike's circle. Therefore, we can try to represent the Mueller matrix of the objective lens using the Zernike polynomials [24] by taking each element of the Mueller matrix as a pseudo optical pupil. Based on the circular symmetry characteristics of the polarization effect of the objective lens found in the previous research and the ease of calibration, when calibrating the objective lens, we actually calibrate a diameter of the objective lens, and then expand the polarization effect of the entire objective lens through the form of rotational symmetry. As a reminder, the Zernike polynomials are used as a set of orthogonal basis functions from the point of view of a pure mathematical operation, and there is no physical meaning.

The constituent materials of the objective lens are assumed to be reciprocal and isotropic. The objective lens selected in the system is stress-free. The off-line measurement shows that the polarization effect mainly comes from the beam redirection, and the birefringence effect is small and can be ignored. Therefore, the Mueller matrix of the objective lens can be represented by two independent parameters the amplitude ratio  $\Psi_{OL}$  and phase difference  $\Delta_{OL}$ :

$$\Psi_{OL}(\rho, \xi) = \sum_{l=1}^L f_l(\rho_k, \xi_k) Z_{l,\Psi} + \varepsilon_{k,\Psi} \quad (k = 1, 2, \dots, K), \quad (7a)$$

$$\Delta_{OL}(\rho, \xi) = \sum_{l=1}^L f_l(\rho_k, \xi_k) Z_{l,\Delta} + \varepsilon_{k,\Delta} \quad (k = 1, 2, \dots, K), \quad (7b)$$

where  $K$  is the number of sampling points,  $Z_{l,\Psi}$  and  $Z_{l,\Delta}$  are the coefficients of the  $l$ -th order Zernike polynomial of the corresponding parameter, and  $\varepsilon_{k,\Psi}$  and  $\varepsilon_{k,\Delta}$  are the fitting error of the corresponding parameter.  $(\rho, \xi)$  corresponds to the polar diameter and polar angle in the polar coordinate, and has the following relationship with the incident angle  $\theta$  and azimuth angle  $\varphi$  in the system:

$$\theta = \sin^{-1}\left(\frac{\rho}{\rho_{max}}\right) NA, \quad \varphi = \xi. \quad (8)$$

Among them,  $\rho_{max}=2f_{OL}NA$  is the radius of optical pupil determined by the NA and focal length of the objective lens.

To find out Zernike coefficients that are sensitive to the polarization effect of the objective lens, we decompose the results measured by the offline method [25] and learn that only a few Zernike coefficients are sensitive to the objective lens among the first 49 of them. These coefficients are consistent with the rotationally symmetrical distribution of aberrations, which can be considered as the polarization effect of the objective lens is related to the incident angle. The polynomials corresponding to the Zernike coefficients with a coefficient value greater than 1% (the 1st, 4th, 9th, 16th, 25th, 36th, 42nd, 49th order Zernike coefficients) are selected to describe the polarization effect of the objective lens, and the decomposed data is used as the initial value of the subsequent fitting.

The relationship between the incident angle of illumination and the rotation angle of the mirror need to be calibrated at the same time. According to Abbe's law of sine, the relationship theoretically is a proportional relationship as shown in Eq. (4). However, due to the defect of the instrument optical path and the errors of the hardware, the actual relationship is a linear equation, which can be expressed as:

$$\sin \theta = C \sin 2\eta + D, \quad (9)$$

where  $C$  is the slope and  $D$  is the intercept. The measurement Mueller matrix  $\mathbf{M}_s$  in Eq. (1) under the incident angle  $\theta$  and the azimuth angle  $\varphi$  can be expressed as:

$$\mathbf{M}_s = \mathbf{M}_{bt}(\Psi_{bt}, \Delta_{bt}) \cdot \mathbf{M}_{OL}(\theta, \varphi) \cdot \mathbf{M}_{SiO_2}(\theta) \cdot \mathbf{M}_{OL}(\theta, \varphi) \cdot \mathbf{M}_{br}(\Psi_{br}, \Delta_{br}), \quad (10)$$

where  $\mathbf{M}_{OL}(\theta, \varphi)$  is the Mueller matrix of the high NA objective lens at the incident angle  $\theta$  and the azimuth angle  $\varphi$ , and  $\mathbf{M}_{SiO_2}(\theta)$  is the Mueller matrix of the standard  $SiO_2$  sample with a known nominal thickness at the incident angle  $\theta$ , which can be calculated from the thin film transmission matrix. Therefore, the formula contains 11 unknowns namely: 8 Zernike coefficients (the 1st, 4th, 9th, 16th, 25th, 36th, 42nd, 49th order Zernike coefficients), the slope  $C$ , the intercept  $D$ , and the thickness  $d$  of the standard film sample. Note that  $\mathbf{M}_{bt}(\Psi_{bt}, \Delta_{bt})$  and  $\mathbf{M}_{br}(\Psi_{br}, \Delta_{br})$  have been calibrated in the first step calibration.

The second step calibration adopts a uniform standard  $SiO_2/Si$  film with known optical constants and nominal thickness as the calibration sample. The calibration setup is the same

as the measurement system in Fig. 1. The specific steps are: place the standard sample on the sample stage, control motorized rotating stage to drive the mirror to a certain angle, and then perform the measurement under the condition. Repeat the above steps to obtain a series set of data at different incident angles. The whole optical pupil of the objective lens should be calibrated. A principle for sampling is that when the incident angle is small (the converging point of the imaging lens on the BFP is with the circle corresponding to  $NA = 0.6$ ), the sampling points can be sparse, otherwise the sampling points should be dense. After all measurements, the nonlinear fitting method is still used to calibrate the above 11 unknowns:

$$\arg \min_{\Omega_2} \sum_{i=1}^{J_2} \|\mathbf{M}_{s,i}(\Omega_2) - \mathbf{M}_{c,i}\|_2. \quad (11)$$

Among them,  $J_2$  is the number of rotations of the mirror  $M$ , and the larger the  $J_2$  is, the more accurate the measurement is.  $\mathbf{M}_c$  represents the Mueller matrix obtained by the fitting model. Both  $\mathbf{M}_s$  and  $\mathbf{M}_c$  are functions of the above 11 unknowns. Detailed calibration results are given in Appendix B.

#### 4. System performances

##### 4.1. Sub-micro lateral resolution

Figure 4 presents the test results for the lateral resolution of the IMME. The measurement on the 1951 high-resolution test target (#55-622, Edmund Optics, Inc., USA) shows that the IMME can distinguish the second smallest line pair at wavelength of 700 nm, suggesting that the corresponding lateral resolution is better than 0.87  $\mu\text{m}$ . The IMME can distinguish the smallest line pair at wavelength of 690 nm, as illustrated in Fig. 4(a), indicating the corresponding lateral resolution is better than 0.78  $\mu\text{m}$ . Figure 4(b) shows imaging resolution results measured by modulation transfer function (MTF) test target. It is generally believed that when the modulation factor is less than 5%, the corresponding line pair is the smallest one that the system can distinguish. From Fig. 4(b), when modulation factor is 5%, the line pair is 1250 lp/mm at wavelength of 700 nm, which again suggests the resolution of the IMME reaches to 0.8  $\mu\text{m}$ .

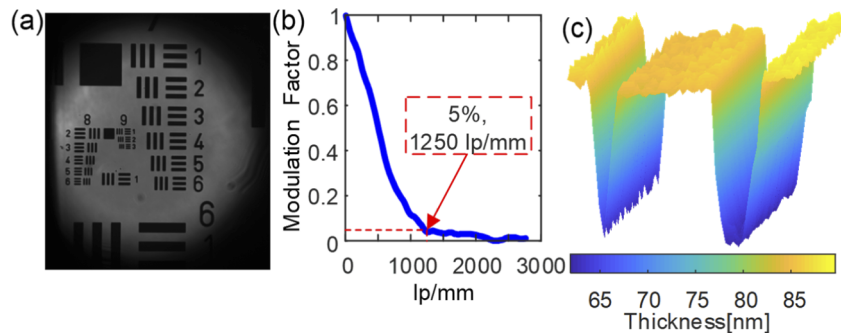


**Fig. 4.** Test results for the lateral resolution of the IMME: (a) image of the 1951 USAF high-resolution test target at wavelength of 690 nm; (b) modulation factor measured with the MTF test target at wavelength of 700 nm; (c) extracted profile result of 1  $\mu\text{m}$  and 3  $\mu\text{m}$  etched trenches.

To further evaluate the lateral resolution of the developed IMME, we designed and fabricated test samples of  $\text{SiO}_2$  etched trenches with different widths on the silicon substrate (single crystal silicon). There are 10  $\text{SiO}_2$  trench structures uniformly etched on the silicon substrate. The lines whose nominal widths are 1  $\mu\text{m}$  and 3  $\mu\text{m}$  are measured to evaluate the instrument. The

measurement was performed at wavelength of 410 nm to 700nm, and from Fig. 4(c), it can be seen that for the two grooves, the measurement results include data in multiple pixels, so the instrument can achieve a lateral resolution of better than 1  $\mu\text{m}$ . Due to the large collection angle of the IMME, the scattered light at the edge of the groove will be collected. This is the reason why the height of the edge may not change vertically.

#### 4.2. Hadamard mode imaging

In order to quickly and accurately identify the difference between samples, it is necessary to use the contrast mode for observation. In general, the information of sample contrast can be obtained by the imaging Mueller matrix. The contrast is defined as  $\text{Contrast} = (M_{ij,\text{sub}} - M_{ij,\text{sample}})/(M_{ij,\text{sub}} + M_{ij,\text{sample}})$ . Here,  $M_{ij,\text{sub}}$  and  $M_{ij,\text{sample}}$  are values of Mueller matrix elements in row  $i$  and column  $j$  ( $i, j = 1, 2, 3, 4$ ) of substrate and sample respectively. However, in some cases, due to the insufficient contrast of the elements of the Mueller matrix, it is difficult to identify all the characteristic differences of the sample. Here, we propose an intensity mode, referred to as *Hadamard mode imaging mode*, to identify the micro-area of the materials and to find the area to be measured with IMME. In Hadamard mode imaging, an intensity image of the sample is recorded for a specific polarization state with maximum contrast between sample and substrate. The contrast is defined as  $\text{Contrast} = (H_{j,\text{sub}} - H_{j,\text{sample}})/(H_{j,\text{sub}} + H_{j,\text{sample}})$ . Here,  $H_{j,\text{sub}}$  and  $H_{j,\text{sample}}$  are values of the  $j$ -th Hadamard components of substrate and sample, respectively.

Next, we will use an example to compare the contrast between Hadamard component and Mueller matrix in a specific situation. A monocrystalline MoS<sub>2</sub>/glass sample was measured and the results are shown in Fig. 5. The experiment was performed at wavelength of 633 nm and incident angle of 60°. In one optical period, we collected 50 Hadamard components. The Hadamard component ( $H_{13}$ ) and the Mueller matrix element ( $M_{34}$ ) with best contrast were chosen by examining all components. The image of the sample is presented as insert in Fig. 5. The data of the pixels on the red dotted line are used to calculate the contrast. It can be seen that under the same systematic condition, the Hadamard component shows a contrast about 4 times higher than the Mueller matrix element. The images obtained under different polarization states have different contrasts [26]. In an optical period, different Hadamard components actually correspond to different polarization states. In the process of calculating the Mueller matrix, all Hadamard components are used, so the contrast displayed in the Mueller matrix image is actually a homogenization effect of the contrast in the Hadamard component, and some specific sample information may be invisible. Therefore, by appropriately selecting the Hadamard component, it is possible to show a higher contrast than the Mueller matrix.

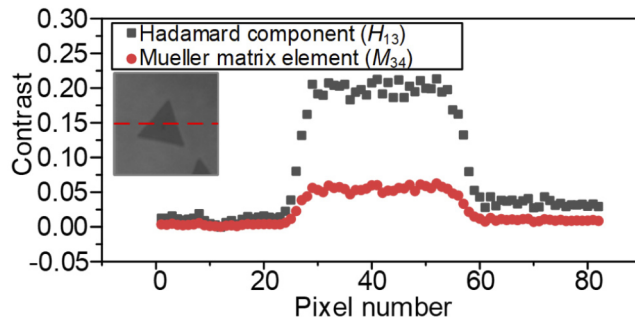


**Fig. 5.** Contrast (corresponding to the red dotted line in the insert) comparison of imaging Mueller matrix element ( $M_{34}$ ) and Hadamard component (the 13th).

#### 4.3. Film thickness measurement

Thin film thickness measurement is often used as a validation tool for the performance of ellipsometry. In order to verify the measurement accuracy of the proposed IMME, a series of SiO<sub>2</sub>/Si thin films with different thicknesses were measured. The measurement results of the proposed method are compared with reference thickness values obtained from a commercial spectroscopic ellipsometer (ME-L, Wuhan Eoptics, Co., Ltd, China).

Figure 6 shows the fitting results between the measured curves and fitting curves calculated by the theoretical model of the SiO<sub>2</sub>/Si thin film sample with a nominal thickness of 25 nm at wavelength of 410 nm – 700 nm and at incident angle of 60°. The measured curves and fitting curves match well, which means that through the proposed method, the parameters and polarization effects of each component in the system have been accurately calibrated. Table 1 summarizes thickness measurement results including 95% confidence limits of five SiO<sub>2</sub>/Si films by the IMME and the commercial Mueller matrix ellipsometer. The deviations in the thicknesses measured by the IMME are within 2.5% compared with results of the commercial Mueller matrix ellipsometer. To evaluate the match performance, the root mean square error (RMSE) between the Mueller matrix measurement spectrum and the theoretical Mueller matrix spectrum corresponding to the measured parameter [27] is calculated.

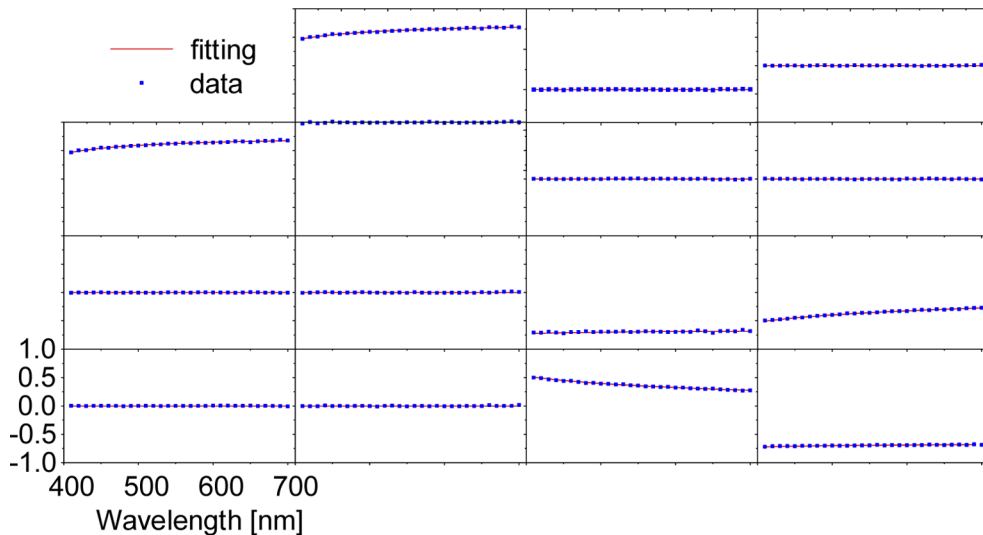


**Fig. 6.** Measured and fitting results of the SiO<sub>2</sub>/Si thin film sample with thickness of 25 nm at wavelength of 410 nm – 700 nm and incident angle of 60 °

**Table 1. Thickness measurement results of the five SiO<sub>2</sub>/Si samples (95% confidence limits)**

| Nominal thickness [nm] | IMME [nm]      | Commercial MME [nm] | Deviation | RMSE |
|------------------------|----------------|---------------------|-----------|------|
| 2                      | 1.80 ± 0.145   | 1.76 ± 0.126        | 2.3%      | 3.3  |
| 25                     | 23.45 ± 0.231  | 22.96 ± 0.153       | 2.1%      | 4.1  |
| 64                     | 65.46 ± 0.458  | 64.70 ± 0.243       | 1.2%      | 3.0  |
| 129                    | 127.32 ± 0.891 | 128.12 ± 0.306      | 0.6%      | 3.2  |
| 342                    | 343.27 ± 0.879 | 341.39 ± 0.405      | 0.5%      | 4.5  |

## 5. Applications

### 5.1. Isotropic material: $WS_2$ on glass

Two-dimensional (2D)  $WS_2$  is an in-plane isotropic layered material and has attracted widespread attention and research in the industry due to its superior electrochemical properties [28–30]. The sample measured in this experiment was a CVD monocrystalline  $WS_2$  flake on the glass substrate from Shenzhen Six Carbon Technology Co., Ltd. The sample was measured by the IMME with an incident angle of  $60^\circ$  and wavelength of 410 nm – 700 nm with an interval of 10 nm.

The results calculated from one pixel are presented. The pixel close to the center of the sample while avoiding contaminants is selected, and the data of surrounding pixels of the selected pixel are calculated to ensure the correctness and consistency of results. Figure 7(b) shows the Hadamard component  $H_{13}$ . The size of the measured flake is about 6  $\mu\text{m}$ . Figure 7(a) shows the measured Mueller matrix of the  $WS_2$ /glass sample and the best fitting result. It can be seen that the measured and fitted curves are basically in agreement. The approximate zero of the off-diagonal elements also proves the measurement accuracy of the IMME on the other hand. Through fitting, the measured data can be matched with the theoretical model, and the thickness and optical constants of the 2D  $WS_2$  can be obtained. Figure 7(c) shows the optical constants (the refractive index  $n$  and the extinction coefficient  $k$ ) extracted from the measured data over the wavelength range of 410 nm -700 nm. In the concerned wavelength range, three featured peaks can be observed, which indicates the positions of optical transitions of the 2D  $WS_2$ . The results are consistent with those reported in the literature [31]. The fitted thickness including

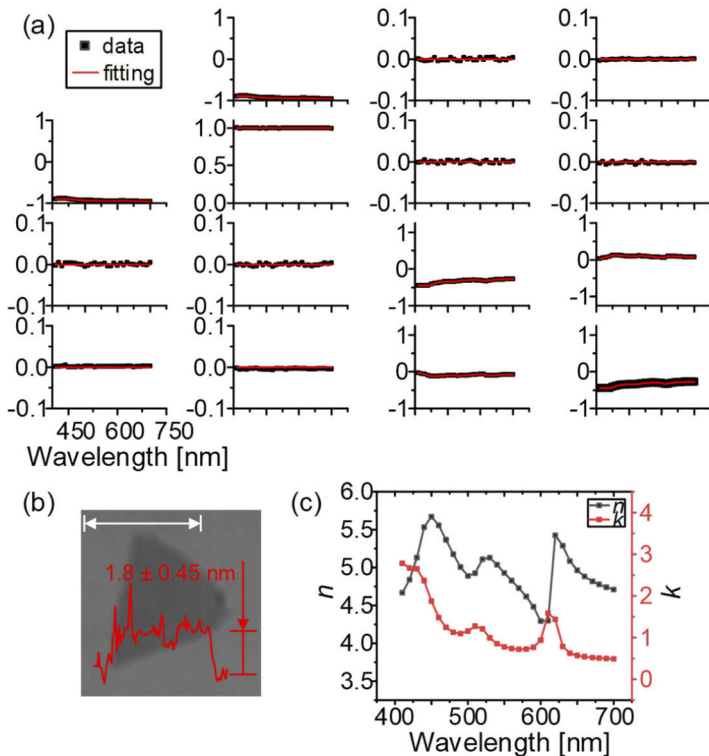


**Fig. 7.** Results of  $WS_2$ /glass sample measured by the IMME: (a) Measured and fitting results; (b) Hadamard mode image and AFM measurement result (the scale bar is 5  $\mu\text{m}$ ); (c) optical constants

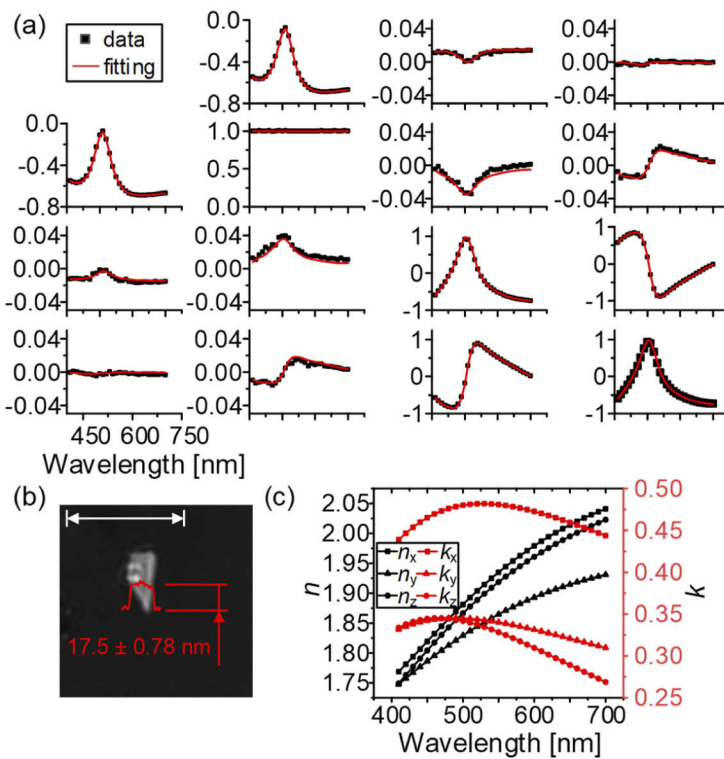


**Fig. 8.** Results of the GeS<sub>2</sub>/glass sample measured by the IMME: (a) Measured and fitting results; (b) Hadamard mode image and AFM measurement result (the scale bar is 5  $\mu\text{m}$ ); (c) optical constants

95% confidence limits is  $1.92 \pm 0.686$  nm. We use the AFM to conduct a comparative test on the measured area, and the thickness obtained is  $1.8 \pm 0.45$  nm. The measurement results of the two techniques basically agree with each other.

### 5.2. Anisotropic material: GeS<sub>2</sub> on glass

2D GeS<sub>2</sub> is a typically in-plane anisotropic layered material with excellent optical and electrical properties [32–33]. The sample measured in this experiment was a GeS<sub>2</sub> flake on the glass substrate from Shenzhen Six Carbon Technology Co., Ltd. The sample was measured by IMME with incident angle of 60°, wavelength of 410 nm – 700 nm at interval of 10 nm and azimuth angles of 0°, 30°, and 60°. Using the data measured under multi-azimuth angles, the information of anisotropic samples can be fitted more accurately.

The results calculated from one pixel are presented. The Hadamard component with the highest contrast are selected as  $H_{28}$ , as shown in Fig. 8(b). The size of the measured flake is about 1.5  $\mu\text{m}$ . Figure 8(a) shows the measured and fitting results of the Mueller matrix of the GeS<sub>2</sub>/glass sample. It can be seen from the off-diagonal elements of the Mueller matrix that the GeS<sub>2</sub> film exhibits obviously optical anisotropy. The results of the measurement and the theoretical model are also approximately in agreement. Among them, the fitting of the two elements  $M_{32}$  and  $M_{23}$  at 580 nm – 700 nm has partial deviations caused by measurement errors. Figure 8(c) shows the measured optical constants of GeS<sub>2</sub>. The GeS<sub>2</sub> is a biaxial crystal, and the optical constants of the three directions are different. The refractive indices in the x and z directions are relatively close in the 410 nm – 700 nm wavelength range, while the refractive index in the y

direction is obviously smaller than those in the other two directions. The refractive indices in all three directions gradually increase as the wavelength increases. The extinction coefficients in the y and z directions are relatively consistent with each other in the wavelength range of 410–500 nm, but the difference gradually increases in the wavelength range of 510–700 nm. The extinction coefficient in the x direction is quite different from those in the y and z directions over the entire measurement wavelength range. The dispersive characteristics of the optical constants of GeS<sub>2</sub> were modeled with Tauc-Lorentz oscillators. The thickness of the sample including 95% confidence limits is  $18.60 \pm 1.325$  nm. The thickness of the sample measured by AFM is  $17.5 \pm 0.78$  nm, basically agreeing with the result of the IMME.

## 6. Conclusion

A new type of imaging Mueller matrix ellipsometry with sub-micron resolution is proposed and developed based on back focal scanning on a high NA (0.95) objective lens. The IMME combines the Mueller matrix ellipsometry with a microscopy, and achieves high-precision ellipsometric measurement under the premise of ensuring high lateral resolution. The key performance indices of IMME are as follows:

- (1) Applicable spectral range: 410 nm -700 nm;
- (2) Range of incident angle: 0° - 65°;
- (3) Range of azimuth angle: 0° - 360°;
- (4) Lateral resolution: better than 0.8 microns (at wavelength of 410 nm – 700 nm).

In order to solve the possible influence of systematic errors on the measurement of the IMME, a two-step calibration method is proposed. Applying the proposed method, the initial azimuth angles of the polarizer and analyzer, the initial azimuth angles and retardance of the two waveplates, the polarization effects of the beam splitter and the high NA objective lens, and the relationship between the incident angle and the rotation angle of the plane mirror have been accurately calibrated.

The proposed IMME has the ability to simultaneously measure the surface topography and optical properties of the sample. The measurement and analysis of a WS<sub>2</sub> sample and a GeS<sub>2</sub> sample were carried out using the developed instrument. Experimental results demonstrate that the proposed IMME has great potential in characterizing samples containing complex features, especially micron-distribution, nano-thickness, optical anisotropy, etc., through high-precision spectroscopic Mueller matrix ellipsometric measurement with sub-micron lateral resolution, multi-incident and multi-azimuth angles.

## Appendix A: Detailed results of the first step calibration method

The results of the first step calibration at wavelength of 410 nm – 700 nm are given here. In the whole range of the light spot, the polarization characteristics are relatively uniform. Therefore, in order to reduce the random noise, the average values of all pixels are taken as the final calibration results. During the fitting process, the measured and fitting Fourier coefficients match well with the root mean square error of 0.52, indicating that the calibration is reliable. Figure 9(a) shows the fitting results of calibrated systematic parameters. The azimuth angles ( $P_p$ ,  $A_p$ ,  $C_1$ ,  $C_2$ ) of the polarizing elements are close to the preset values and the results of all wavelengths are consistent. The retardation curves of the waveplate are basically in line with the design value. Figure 9(b) shows the calibration results of the Mueller matrices of the beam splitter in transmission and reflection modes. It can be seen that the reflection mode of the beam splitter has a greater influence on the system measurement results than the transmission mode of the

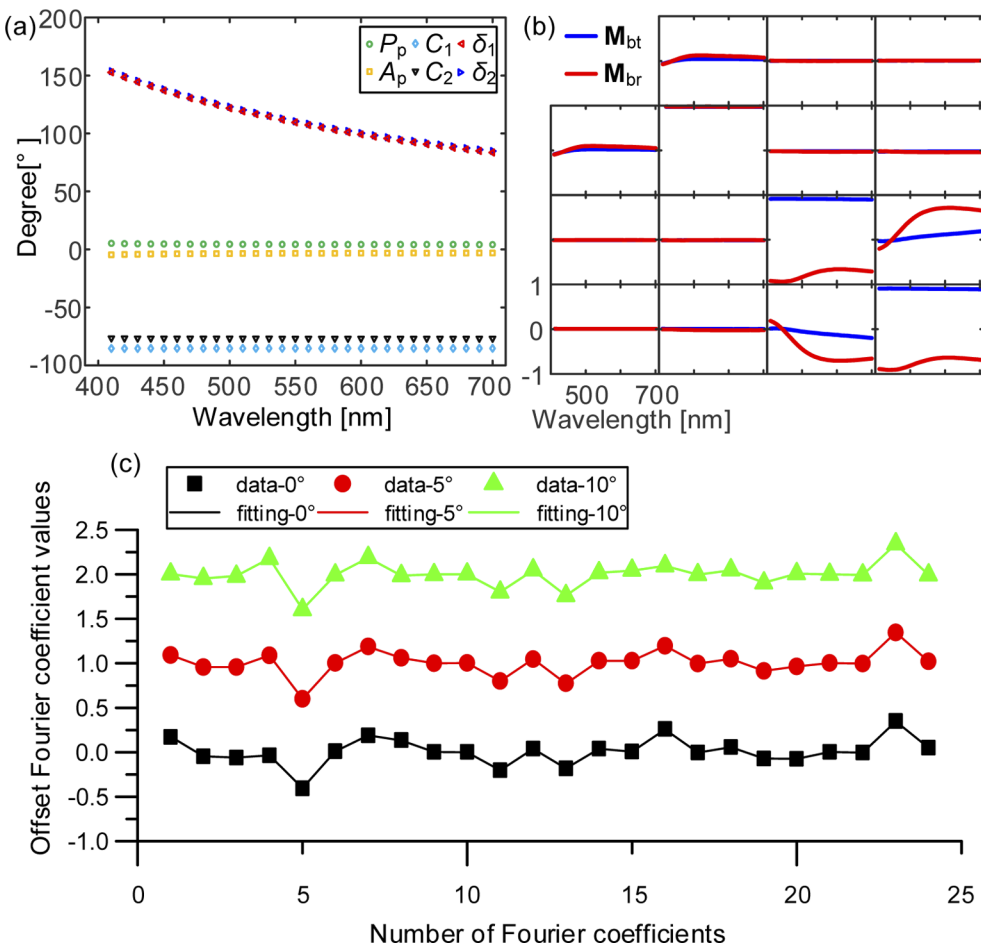


**Fig. 9.** Calibration results of (a) systematic parameters ( $P_p$ ,  $A_p$ ,  $C_1^0$ ,  $C_2^0$ ,  $\delta_1$ ,  $\delta_2$ ) and (b) beam splitter at wavelength of 410 nm – 700 nm by using the first step calibration method; (c) fitting results of the Fourier coefficients in the first step calibration.

beam splitter. In the wavelength range of 410 nm to 540 nm, the polarization characteristics of the beam splitter are more sensitive to the wavelength, while in the wavelength range of 550 nm to 700 nm, it is less sensitive. It is related to the material selection of the beam splitter and the design of the coating films. Figure 9(c) shows the fitting result of the Fourier coefficients in the first step calibration. In order to clearly show the results, the  $5^\circ$  and  $10^\circ$  measurement fitting curves are shifted upward by 1 and 2 unit lengths, respectively. It can be observed that the measured Fourier coefficients fit well with calculated ones using system model, indicating the rationality of the proposed first step calibration method.

#### Appendix B: Detailed results of the second step calibration method

The polarization aberration of the high NA objective lens is illustrated in Fig. 10(a). As seen from the figure, with the NA increasing, the variation range of Mueller matrix increases. This is because closer to the edge of the objective lens, the deflection of light increases, and the influence on the polarized light increases. Figure 10(b) shows the relationship between the incident angle of illumination and the rotation angle of the mirror. The distribution of measuring points is

approximately a linear function curve. When the measurement needs to be carried out at a certain incident angle, the deflection angle of the mirror can be set through the calibrated relationship. Figure 10(c) shows the fitting result of the Mueller matrix in the second step calibration. It can be seen that the measured Mueller matrix fit well with the calculated one using theoretical model, indicating the rationality of the proposed second step calibration method.

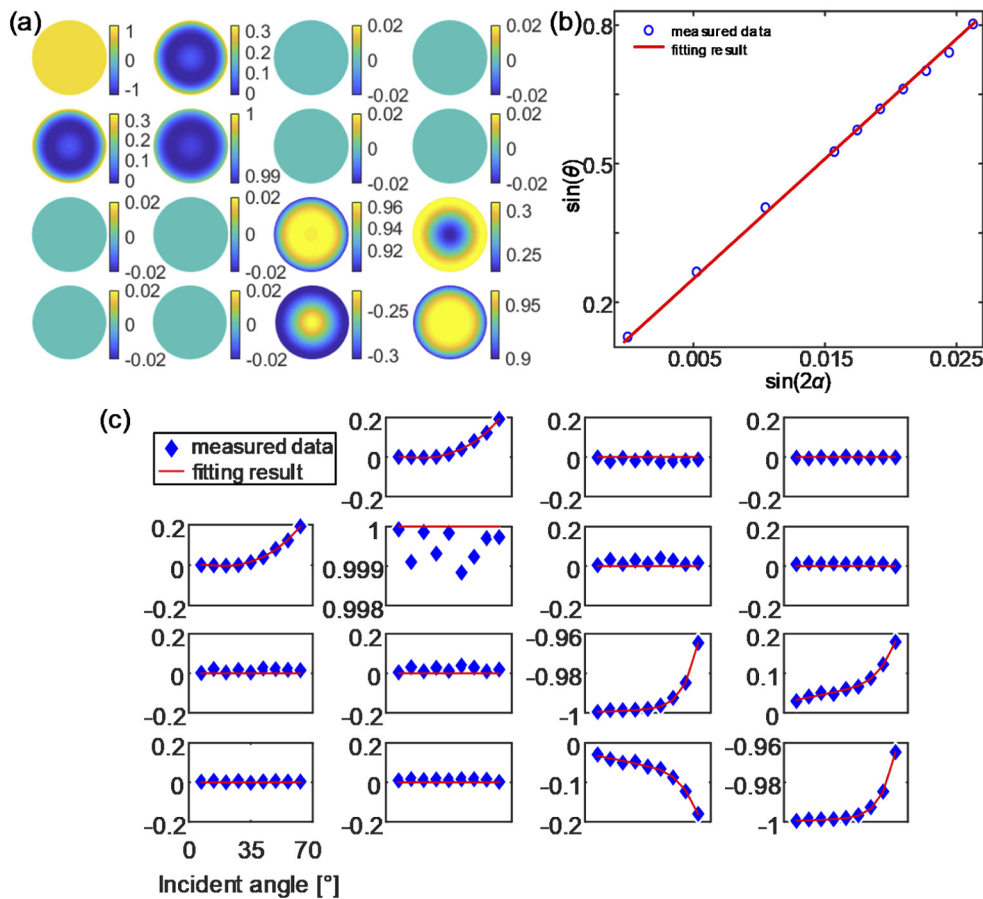


**Fig. 10.** Calibration results of (a) objective lens at wavelength of 630 nm and (b) incident angle by using the second step calibration method; (c) fitting results of the Mueller matrix in the second step calibration.

**Funding.** National Natural Science Foundation of China (51775217, 51727809, 52022034, 51805193); National Major Science and Technology Projects of China (2017ZX02101006-004); Key Research and Development Plan of Hubei Province (2020BAA008).

**Disclosures.** The authors declare that there are no conflicts of interest related to this article.

**Data availability.** Data underlying the results presented in this paper are not publicly available at this time but may be obtained from the authors upon reasonable request.

## References

1. S. Ruby, *Recent Development in Optoelectronic Devices*. (BoD–Books on Demand, 2018).
2. H. N. Hansen, K. Carneiro, H. Haitjema, and L. Chiffre, “Dimensional micro and nano metrology,” *CIRP Annals* **55**(2), 721–743 (2006).
3. A. C. Ferrari, J. C. Meyer, V. Scardaci, and C. Casiraghi, “Raman spectrum of graphene and graphene layers,” *Phys. Rev. Lett.* **97**(18), 187401 (2006).

4. T. Li, A. J. Senesi, and B. Lee, "Small angle X-ray scattering for nanoparticle research," *Chem. Rev.* **116**(18), 11128–11180 (2016).
5. R. M. A. Azzam and N. M. Bashara, *Ellipsometry and Polarized Light*. (Amsterdam, 1977).
6. H. K. Tompkins and E. A. Irene, *Handbook of Ellipsometry*. (Springer, 2005).
7. H. Fujiwara, *Spectroscopic Ellipsometry: Principles and Applications*. (Wiley, 2007).
8. G. Jin, R. Jansson, and H. Arwin, "Imaging ellipsometry revisited: Developments for visualization of thin transparent layers on silicon substrates," *Rev. Sci. Instrum.* **67**(8), 2930–2936 (1996).
9. Y. Kajihara, K. Fukuzawa, S. Itoh, and H. Zhang, "Real-Time visualization of a shearing nanometer-thick lubricant film by two-stage imaging ellipsometric microscopy," *IEEE Trans. Magn.* **47**(10), 3441–3444 (2011).
10. D. H. Kim, Y. H. Yun, and K. N. Joo, "LASIE: large area spectroscopic imaging ellipsometry for characterizing multi-layered film structures," *Int. J. Precis. Eng. Manuf.* **19**(8), 1125–1132 (2018).
11. E. Shoji, A. Komiya, J. Okajima, M. Kubo, and T. Tsukada, "Three-step phase-shifting imaging ellipsometry to measure nanofilm thickness profiles," *Opt. Laser Eng.* **112**, 145–150 (2019).
12. O. Arteaga, M. Baldríz, J. Antó, A. Canillas, E. Pascual, and E. Bertran, "Mueller matrix microscope with a dual continuous rotating compensator setup and digital demodulation," *Appl. Opt.* **53**(10), 2236–2245 (2014).
13. Y. Wang, H. He, J. Chang, C. He, S. Liu, M. Li, N. Zeng, J. Wu, and H. Ma, "Mueller matrix microscope: A quantitative tool to facilitate detections and fibrosis scorings of liver cirrhosis and cancer tissues," *J Biomed. Opt.* **21**(7), 071112 (2016).
14. K. Namba, K. Fukuzawa, S. Itoh, H. Zhang, and N. Azuma, "Extension of measurement range of lubrication gap shape using vertical-objective-type ellipsometric microscopy with two compensator angles," *Tribol. Int.* **142**, 105980 (2020).
15. K. Fukuzawa, Y. Sasao, K. Namba, C. Yamashita, S. Itoh, and H. Zhang, "Measurement of nanometer-thick lubricating films using ellipsometric microscopy," *Tribol. Int.* **122**, 8–14 (2018).
16. O. Arteaga, S. M. Nichols, and J. Antó, "Back-focal plane Mueller matrix microscopy: Mueller conoscopy and Mueller diffractrometry," *Appl. Surf. Sci.* **421**, 702–706 (2017).
17. W. Shen, C. Hu, J. Tao, J. Liu, S. Fan, Y. Wei, C. An, J. Chen, S. Wu, Y. Li, J. Liu, D. Zhang, L. Sun, and X. Hu, "Resolving the optical anisotropy of low-symmetry 2D materials," *Nanoscale* **10**(17), 8329–8337 (2018).
18. S. W. Lee, G. Choi, S. Y. Lee, Y. Cho, and H. J. Pahk, "Coaxial spectroscopic imaging ellipsometry for volumetric thickness measurement," *Appl. Opt.* **60**(1), 67–74 (2021).
19. S. W. Lee, S. Y. Lee, G. Choi, and H. J. Pahk, "Co-axial spectroscopic snap-shot ellipsometry for real-time thickness measurements with a small spot size," *Opt. Express* **28**(18), 25879–25893 (2020).
20. G. Choi, S. W. Lee, S. Y. Lee, and H. J. Pahk, "Single-shot multispectral angle-resolved ellipsometry," *Appl. Opt.* **59**(21), 6296–6303 (2020).
21. H. Gu, X. Chen, H. Jiang, Y. Shi, and S. Liu, "Wide field-of-view angle linear retarder with ultra-flat retardance response," *Opt. Lett.* **44**(12), 3026–3029 (2019).
22. S. Liu, X. Chen, and C. Zhang, "Development of a broadband Mueller matrix ellipsometer as a powerful tool for nanostructure metrology," *Thin Solid Films* **584**, 176–185 (2015).
23. J. Li, B. Ramanujam, and R.W. Collins, "Dual rotating compensator ellipsometry: Theory and simulations," *Thin Solid Films* **519**(9), 2725–2729 (2011).
24. M. Born and E. Wolf, *Principles of Optics*, 7th ed. (Cambridge University, 1999).
25. C. Chen, X. Chen, H. Gu, H. Jiang, C. Zhang, and S. Liu, "Calibration of polarization effect of a high-numerical-aperture objective lens with Mueller matrix polarimetry," *Meas. Sci. Technol.* **30**(2), 025201 (2019).
26. K. O'Holleran and S. Michael, "Polarization effects on contrast in structured illumination microscopy," *Opt. Lett.* **37**(22), 4603–4605 (2012).
27. B. Song, H. Gu, S. Zhu, H. Jiang, X. Chen, C. Zhang, and S. Liu, "Broadband optical properties of graphene and HOPG investigated by spectroscopic Mueller matrix ellipsometry," *Appl. Surf. Sci.* **439**, 1079–1087 (2018).
28. L. Cheng, W. Huang, Q. Gong, C. Liu, Z. Liu, Y. Li, and H. Dai, "Ultrathin WS<sub>2</sub> nanoflakes as a high-performance electrocatalyst for the hydrogen evolution reaction," *Angew. Chem.* **126**(30), 7994–7997 (2014).
29. N. Perea-López, A. L. Elías, A. Berkdemir, A. Castro-Beltran, H. Gutiérrez, S. Feng, R. Lv, T. Hayashi, F. López-Urías, S. Ghosh, B. Muchharla, S. Talapatra, H. Terrones, and M. Terrones, "Photosensor device based on few-layered WS<sub>2</sub> films," *Adv. Funct. Mater.* **23**(44), 5511–5517 (2013).
30. D. Ovchinnikov, A. Allaïn, Y. S. Huang, D. Dumcenco, and A. Kis, "Electrical transport properties of single-layer WS<sub>2</sub>," *ACS Nano* **8**(8), 8174–8181 (2014).
31. G. H. Jung, S. Yoo, and Q. H. Park, "Measuring the optical permittivity of two-dimensional materials without a priori knowledge of electronic transitions," *Nanophotonics* **8**(2), 263–270 (2018).
32. S. Le Roux and P. Jund, "Ring statistics analysis of topological networks: New approach and application to amorphous GeS<sub>2</sub> and SiO<sub>2</sub> systems," *Comp. Mater. Sci.* **49**(1), 70–83 (2010).
33. Y. Yang, S. C. Liu, X. Wang, Z. Li, Y. Zhang, G. Zhang, D. Xue, and J. Hu, "Polarization-sensitive ultraviolet photodetection of anisotropic 2D GeS<sub>2</sub>," *Adv. Funct. Mater.* **29**(16), 1900411 (2019).